Chapter 4

Analytical Prediction for Grain Burn Time and Burning Area Kinematics in a Solid Rocket Combustion Chamber

Charles A. Osheku, Oluleke O. Babayomi and Oluwaseyi T. Olawole

Additional information is available at the end of the chapter

http://dx.doi.org/10.5772/intechopen.82822

Abstract

This chapter proposes the application of Newtonian particle mechanics for the derivation of predictive equations for burn time, burning and unburnt area propagation for the case of a core propellant grain. The grain is considered to be inhibited in a solid rocket combustion chamber subject to the assumption that the flame propagation speed is constant for the particular solid fuel formulation and formation chemistry in any direction. Here, intricacies surrounding reaction chemistry and kinetic mechanisms are not of interest at the moment. Meanwhile, the physics derives from the assumption of a regressive solid fuel pyrolysis in a cylindrical combustion chamber subject to any theoretical or empirical burn rate characterization law. Essential parametric variables are expressed in terms of the propellant geometrical configuration at any instantaneous time. Profiles from simulation studies revealed the effect of modulating variables on the burning propagation arising from the kinematics and ordinary differential equations models. In the meantime, this mathematical exercise explored the tendency for a tie between essential kernels and matching polynomial approximations. In the limiting cases, closed form expressions are couched in terms of the propellant grain geometrical parameters. Notably, for the fuel burn time, a good agreement is observed for the theoretical and experimental results.

Keywords: solid rocket fuel, tubular rocket propellant, differential equations, burn rate

1. Introduction

Since the advent of rocketry, researchers have preoccupied their minds on the development of effective solid fuels for rocket and missile propulsion systems. A compendium of scholarly

works in propellant chemistry, aerothermodynamics, flight mechanics, guidance, navigation and control analyses abound in the literature. Solid fuels have been and are still in high demand for space mission and missile development planning. Notwithstanding the progresses in solid fuels physics and the advent of huge numerical studies, analytical conjectures are aptly handy for novel mechanical maneuvering of flight trajectories.

In the meantime, considerable progress was made by Tseng and Yang [1] in investigating the combustion of homogeneous propellants in realistic motor environments. The impact of the dispersion of instability signatures into the burning regions on combustion characteristics of the propellant was investigated. On this note, Roh et al. [2, 3] studied in details the relationship between acoustic oscillations and fast changing propellant burning in laminar flows. While the purpose of the study was to discover the underlying causes of perturbations, the inclusion of chemical characteristics provided a more robust mathematical solution. As a matter of scientific fact, same analysis was extended to incorporate the effect of turbulence [4, 5].

Likewise, a comprehensive numerical analysis was conducted in [6] to study the combustion of a double-base homogeneous propellant in a rocket motor. Emphasis was placed on the motor internal flow development and its influence on propellant combustion. The formulation was based on the Favre-averaged, filtered equations for the conservation laws and took into account finite-rate chemical kinetics and variable thermophysical properties. Nonetheless, results from the study showed that a smoother axial velocity gradient in conjunction with a vertical flow convection have a tendency to prevent or circumvent turbulence regime from deep penetration into the primary flame zone. These turbulence energy spectra have prompted dominant harmonics in a frequency range capable of triggering combustion instabilities. Meanwhile, a methodology for the solution of the internal physics of solid propellant rocket motors was described in [7]. The mathematical problem involved the simulation of a burning surface that dynamically changed the interface between the solid propellant and combustion gas phases.

An additional study in [8] showed how a technique was developed to obtain a burning rate data across a range of pressures from ambient to 345 MPa. It combines the uses of a low loading density combustion bomb with a high loading density closed bomb procedure. Furthermore, a series of nine ammonium perchlorate (AP)-based propellants were used to demonstrate the uses of the technique in comparison to the neat AP burning rate barrier. The effect of plasticizer, oxidizer particle size, catalyst and binder type was investigated. This necessitated an experimental program that was performed at the Space Propulsion Laboratory of the Politecnico di Milano. Notably, within the explored operating conditions and the associated uncertainty bands, a neutral trend for the solid fuel regression rate with increasing pressure was observed. The formulation tested was hydroxyl-terminated polybutadiene in gaseous oxygen at pressures ranging from 4 to 16 bars. A simplified analytical model, which retains the essential physics and accounts for pressure dependency, was developed for hybrid rockets in conjunction with the corresponding numerical simulation reported in [9]. However, the results of its simplified analytical model may not translate directly for use with solid rockets.

Nonetheless, the study reported in [10] was concerned with the prediction of the pressure history during the process of flame-spreading and combustion of solid propellant grains as

http://dx.doi.org/10.5772/intechopen.82822

would occur, for example, in a gun cartridge. Solution of the governing conservation equations for the two-phase media requires the use of empirical relations to account for the physical processes of momentum and energy interaction between the solid grains and hot propellant gas. The results indicated the significance of these interactions for the predictions of pressure and velocity fields. Of note too is the study in [11], where the combustion response of homogeneous and heterogeneous solid propellants to an imposed velocity field was certified to be a viable model for erosive burning mechanism. This leads to an imposed velocity field that has its roots in a multistate analysis of a solid rocket motor combustion processes. In the meantime, for homogeneous solid propellants, it has been shown that for certain realistic choices of the parameters, both positive and negative erosions simultaneously occurred. The underlying mechanism for erosive burning is tied flame stretching. On the hand, for heterogeneous solid propellants, any enhancements of the burn rate are tied to the cross flow velocity, propellant morphology and geometry and chamber pressure.

While information on thermodynamics is readily available in the literature, very clear analytical representation of the burn time of any geometry is rare. For now a gap exists for theoretical closed form results and experiential validation investigations. Theoretical equations that predict analytical burn time, thermal stresses buildup and how they are related ab initio to the solid propellant geometry are rare in literature. It is therefore necessary to have simplified analytical models that reduce computational time and laborious procedures and having reliance on numerically complicated methods such as computational fluid dynamics (CFD) or computational heat transfer (CHT) that would be utilized in the estimation of the burn time.

Traditionally, design and analysis of solid rocket motors have relied on empirical measurements to characterize fuel burn times and other propellant/motor performance quantities. This has been primarily because of the complexity of modeling adequately nontrivial fuel grain geometries and combustion processes. As overall system and vehicle performance models become more advanced and answer greater demands in terms of accuracy and detail, it is increasingly necessary to include more sophisticated models of subsystems such as the rocket motor. On the other hand, improved computational capabilities and better insights gleaned from experimental studies provide the means of achieving these better subsystem models. This chapter therefore covers a topic that is ripe for study and has potential to be of significant use to engineers who need to model burning performance for solid rocket propulsion. It may be of particular interest to those who lack the luxury of pursuing an experimental test campaign for a range of candidate fuel grain designs and parameters.

Several competing approaches exist in recent literature based on different focuses in terms of fundamental physics: analysis of radiation, temperature distribution and a range of coupled fluid flow/combustion approaches of varying complexity from 1D flow models to CFD. The method proposed in this chapter is beneficial in terms of its simplicity and consequently low computational cost, although its significant central assumptions mean that it can be applied only to certain cases (homogeneous propellants, tubular (regressive) grain designs and constant regression rates/steady-state operation). Its focus on only the kinematic viewpoint, without accounting for minutiae of chemical kinetic mechanisms, appears fairly unique among recent studies which have instead delved into the physically dominant processes at work.

Predicting grain burn time and burning area kinematics can be done in three ways: empirically (by experiment), analytically (using approximated mathematical models solved exactly) or numerically (by applying exact mathematical models solved approximately). The method proposed in the chapter falls into two parts: the first (burning time determination) combines analysis for modeling supplemented by empirical test data; the second part (burning/unburnt area determination) only covers an analytical approach without experimental or numerical validation [12].

The chapter is organized as follows: first is the derivation of the burn time equation, followed by an analysis of the effects of multiple points of ignition on the burn time. Analytical models are developed for unburnt and burning area propagation and discussion of results and the conclusion.

2. Derivation of burn time equation

In this section, the theory conjured is subject to the under listed assumptions, namely:

i. Propellant is homogeneous with uniform grain geometry.

ii. Any characterization burning rate law applies.

iii. After ignition, simultaneous burning process ensues along specified directions with constant regression rates. The alternative model, in [13], focuses on transient conditions and also describes erosive burning, which may be of interest in contrast to the erosive burning that can be accounted for in this chapter's proposed method based on kinematics. One evident advantage of this chapter's proposal is that it does not require any calculation of the fluid flow field, whereas even the alternative simplified 1D flow calculation proposed in [14] necessitates further computational expense, potentially.

iv. Inner tubular burning characterizes the process.

The typical tubular propellant and the combustion propagation are illustrated in **Figures 1** and **2**, while **Figure 3** gives an analytical model of the flame particle traversing in the designated axes.

In general, the average value of any time-dependent function $F_0(t)$ within the time interval t_H and t_G satisfies any of the equations:

$$F_{0(avg)} = \frac{1}{(t_G - t_H)} \int_{t_H}^{t_G} F_0(t)dt \tag{1}$$

$$\dot{F}_{0(avg)} = \frac{1}{(t_G - t_H)} \int_{t_H}^{t_G} \left(\frac{dF_0(t)}{dt}\right) dt \tag{2}$$

Given that, (W, L, A_s) are the web (thickness), length (L) and the sectorial area (A_s) of any typical tubular propellant grain, where the following holds:

http://dx.doi.org/10.5772/intechopen.82822

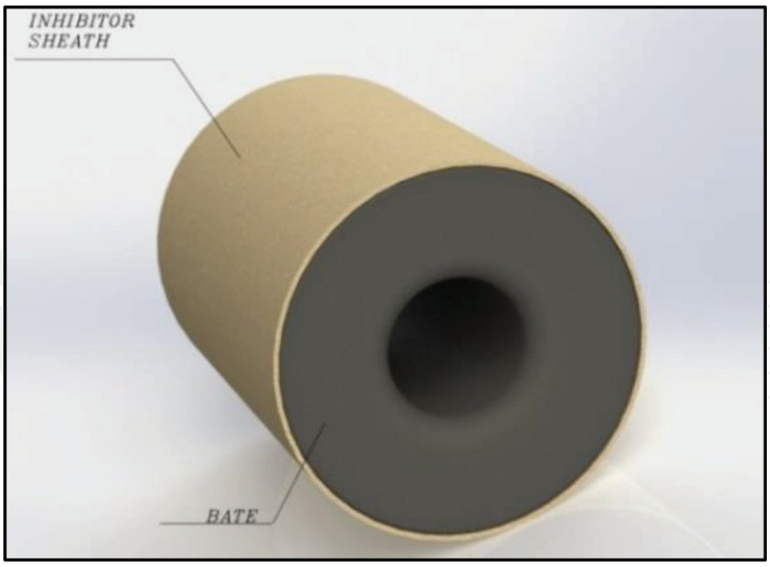

Figure 1. Typical tubular solid fuel.

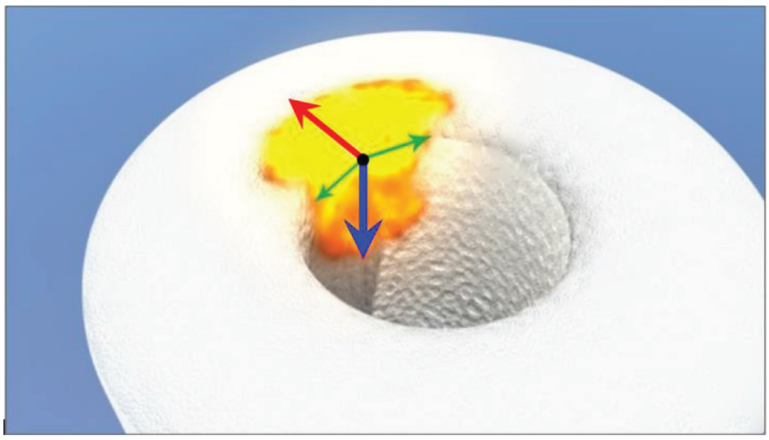

Figure 2. Illustration of different burning directions at point of ignition.

$$(W, L, A_s) \in F_o(t); \left(\dot{W}, \dot{L}, \dot{A}_s\right) \in \dot{F}_o(t)$$

Consequently, the total time required for the entire burning process specified in **Figure 4** must satisfy the following kinematic equation, namely:

$$t_{b(total)} = \frac{W}{\dot{W}} + \frac{L}{\dot{L}} + 2\frac{A_s}{\dot{A}_s} \tag{3}$$

From the point of ignition, as illustrated in **Figure 2**, the following further holds:

$$W = W_o - \dot{r}t_{b(web)}; L = L_o - \dot{r}t_{b(axial)}; d = \mathrm{d}_o + 2\dot{r}t_{b(radial)} \tag{4}$$

$$\|W\| = \left\|W_o - \dot{r}t_{b(web)}\right\|; \|L\| = \left\|L_o - \dot{r}t_{b(axial)}\right\|; \|d\| = \left\|d_o + 2\dot{r}t_{b(radial)}\right\| \tag{5}$$

in conjunction with a constant regression rate $(\dot{r})$. Under these circumstances, Eq. (3) now becomes

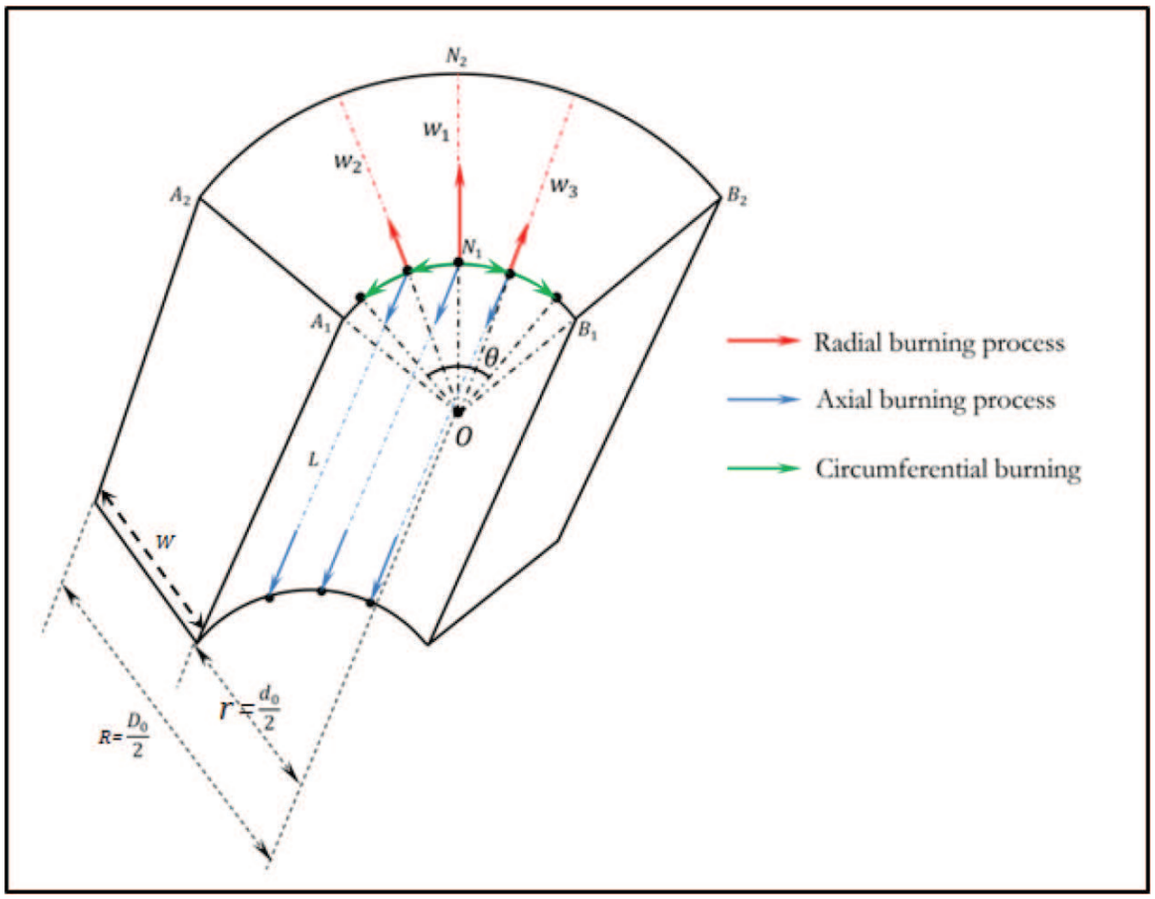

Figure 3. Regression along burn regions.

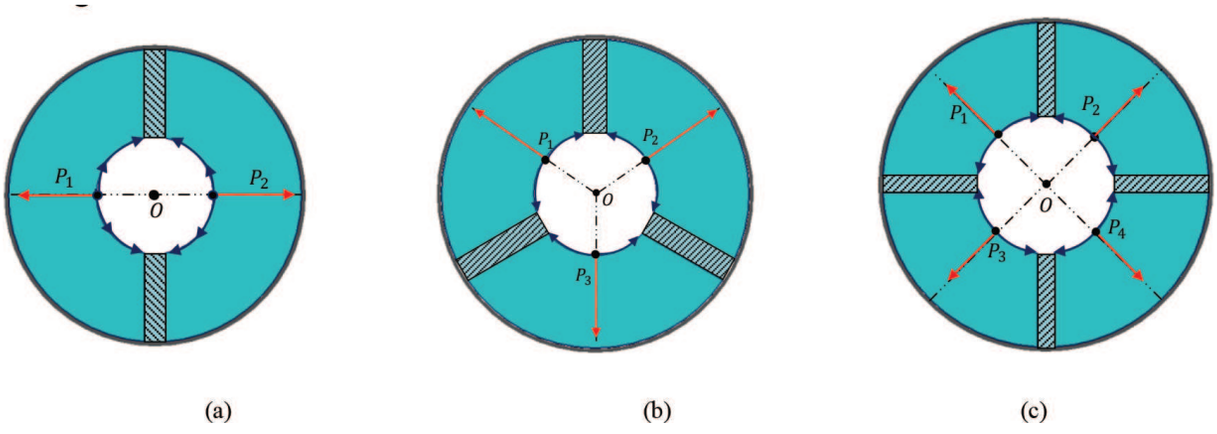

Figure 4. Illustrations of integral part of multiple ignition points on propellant grain. (a) 2-points, (b) 3-points, and (c) 4-points.

$$t_{b(total)} = \frac{W(1+2\eta)+\eta d}{\dot{r}} + 2\frac{A_s}{\dot{A}_s}; \quad \eta = \frac{L}{D} \tag{6}$$

From the sector burning area configuration, the following ensues, viz.:

http://dx.doi.org/10.5772/intechopen.82822

$$A_S = \frac{1}{2}\left(R^2 - r^2\right)\theta = \frac{1}{2}W(W+d)\theta \quad ; \quad \dot{A}_S = \frac{1}{2}\left[\dot{\theta}W(W+d) - \theta d\dot{r}\right] \tag{7}$$

where θ is in radians, in conjunction with the following kinematics relation, viz.:

$$\dot{R} = 0; \dot{r} = \dot{r}_0; \forall\ \ddot{r} = 0 \tag{8}$$

leading to the total segmental burn time for the sectorial propellant grain as

$$\frac{A_s}{\dot{A}_s} = \frac{1}{\dot{r}}\left(\frac{(W+d)\theta}{4\eta\left(1+\frac{W}{d}\right) - \frac{\theta d}{W}}\right) \tag{9}$$

From Eq. (9), Eq. (6) becomes

$$t_{b(total)} = \left(\frac{W(1+2\eta)+\eta d}{\dot{r}} + \frac{2}{\dot{r}}\left(\frac{(W+d)\theta}{4\eta\left(1+\frac{W}{d}\right) - \frac{\theta d}{W}}\right)\right) \quad 0 \le \theta \le 2\pi \tag{10}$$

In the meantime, Eq. (9) in terms of the instantaneous burning time t_ε takes the form, viz.

$$t_{b(total)} = \frac{1}{\dot{r}}\left\{((1+2\eta)W_0 + \eta d_0) - t_\varepsilon + 2\left(\frac{(W_0+d_0)\theta_0 + (W_0+d_0)\dot{\theta}t_\varepsilon + \theta_0\dot{r}t_\varepsilon + \dot{\theta}\dot{r}t_\varepsilon^2}{4\eta\left(1+\frac{W_0-\dot{r}t_\varepsilon}{d_0+2\dot{r}t_\varepsilon}\right) - \left(\frac{d_0\theta_0+\left(2\dot{r}\theta_0+\dot{\theta}d_0\right)t_\varepsilon+2r\dot{\theta}t_\varepsilon^2}{W_0-\dot{r}t_\varepsilon}\right)}\right)\right\} \tag{11}$$

arising from the following flame additional kinematics relations, namely, $\theta = \theta_0 + \dot{\theta}t_\varepsilon$, in conjunction with others specified in Eq. (5).

It is significant to examine the limiting case of Eq. (11) as $t_\varepsilon \to 0$, viz.:

$$\lim_{t_\varepsilon \to 0} t_{b(total)} = \lim_{t_\varepsilon \to 0}\frac{1}{\dot{r}}\left\{((1+2\eta)W_0 + \eta d_0) - t_\varepsilon + 2\left(\frac{(W_0+d_0)\theta_0 + (W_0+d_0)\dot{\theta}t_\varepsilon + \theta_0\dot{r}t_\varepsilon + \dot{\theta}\dot{r}t_\varepsilon^2}{4\eta\left(1+\frac{W_0-\dot{r}t_\varepsilon}{d_0+2\dot{r}t_\varepsilon}\right) - \left(\frac{d_0\theta_0+\left(2\dot{r}\theta_0+\dot{\theta}d_0\right)t_\varepsilon+2r\dot{\theta}t_\varepsilon^2}{W_0-\dot{r}t_\varepsilon}\right)}\right)\right\}$$

$$= \frac{1}{\dot{r}}\left\{\left[\left(1+2\eta_0\right)W_0 + \eta d_0\right] + \left(\frac{2(W_0+d_0)\theta_0}{4\eta\left(1+\frac{W_0}{d_0}\right) - \frac{d_0\theta_0}{W_0}}\right)\right\}; \forall\ \eta = \eta_0 - \frac{\dot{r}t_\varepsilon}{d_0+2W_0}; \eta_0 = \frac{L_0}{d_0+2W_0} \tag{12}$$

to indicate the closed form burn time prediction in terms of the tubular initial geometrical configuration.

In the meantime, Eqs. (10) and (11) are expressed further as

$$t_{b(total)} = \frac{d}{\dot{r}}\left\{[(1+2\eta)\chi + \eta] + \left(\frac{2(1+\chi)\overline{\theta}_0}{4\eta(1+\chi) - \frac{\overline{\theta}_0}{\chi}}\right)\right\};$$

$$\forall\ \chi = \frac{W}{d} = Lt_{t_{\varepsilon=0}}\left(\chi = \frac{W_0 - \dot{r}t_\varepsilon}{d_0 + 2\dot{r}t_\varepsilon}\right) = Lt_{t_{\varepsilon=0}}(\chi) = Lt_{t_{\varepsilon=0}}\left(\frac{\chi_0 - \frac{\dot{r}t_\varepsilon}{d_0}}{1 + \frac{2\dot{r}t_\varepsilon}{d_0}}\right) \tag{13}$$

and

$$t_{b(total)} = \frac{d_0}{\dot{r}}\left\{[(1+2\eta)\chi_0 + \eta] + \left(\frac{2(1+\chi_0)\overline{\theta}_0}{4\eta(1+\chi_0) - \frac{\overline{\theta}_0}{\chi_0}}\right)\right\}\ ;\quad \chi_0 = \frac{W_0}{d_0}\quad ;\quad 0 \le \overline{\theta}_0 \le 2\pi \tag{14}$$

When a propellant is completely burned out $\overline{\theta}_0 = 2\pi$, which corresponds to the case of 1-point ignition, to give the following expression, viz.

$$t_{b(total)} = \frac{d}{\dot{r}}\left\{[(1+2\eta)\chi + \eta] + \left(\frac{\pi(1+\chi)}{\eta(1+\chi) - \frac{\pi}{2\chi}}\right)\right\} \tag{15}$$

When $\overline{\theta}_0 = \pi$, which corresponds to the case of diametric ignition at two opposite sides to give the following expression, viz.

$$t_{b(total)} = \frac{d_0}{\dot{r}}\left\{[(1+2\eta)\chi_0 + \eta] + \left(\frac{\pi(1+\chi_0)}{\eta(1+\chi_0) - \frac{\pi}{2\chi_0}}\right)\right\} \tag{16}$$

This is to be further examined in the subsection for multiple ignition points.

2.1. Effect of multiple ignition points (N_p)

The effect of multiple ignition points is expected to create multiple sectorial flame propagation kinematics as illustrated in the figures below. Here, hatchings are indicating burning surfaces intersection arising from the sectorial kinematic propagation of the flame in line with the description in **Figures 2** and **3**.

Here, the matching kinematic equation takes the form

$$\frac{A_s}{\dot{A}_s}(N_p) = \frac{1}{\dot{r}}\left(\frac{(W+d)\theta_{(N_p)}}{4\eta\left(1+\frac{W}{d}\right) - \frac{\theta_{(N_p)}d}{W}}\right)\forall\ \theta_{(N_p)} = \frac{2\pi}{N_p} \tag{17}$$

It should be noted that propagations in radial and axial directions are expected to be rapid in consonance with the number of ignitions points. The overall effect therefore modulates Eq. (16) as

$$t_{b_{(N_p)}(total)} = \frac{d_0}{\dot{r}}\left\{\left[(1+2\eta)\frac{\chi_0}{N_p} + \frac{\eta}{N_p}\right] + \left(\frac{\frac{\pi}{{N_p}^2}(1+\chi_0)}{\frac{\eta}{N_p}(1+\chi_0) - \frac{\pi}{2\chi_0{N_p}^2}}\right)\right\}$$

http://dx.doi.org/10.5772/intechopen.82822

$$= \frac{d_0}{\dot{r}} \left\{ \left[\left(\frac{1+2\eta}{N_p} \right) \chi_0 + \frac{\eta}{N_p} \right] + \left(\frac{\pi \left(\frac{1+\chi_0}{{N_p}^2} \right)}{\eta \left(\frac{1+\chi_0}{N_p} \right) - \frac{\pi}{2\chi_0 {N_p}^2}} \right) \right\} = \frac{t_{b(total)}}{N_p} \tag{18}$$

3. Unburnt and burning area propagation

The plan and sectional views of the propellant grain geometries are illustrated in the figure below (**Figure 5**). These views are expected to provide illustrations on how the unburnt propellant grain area is derived.

From the figures above, the tubular grain's surface area is given by

$$A_{ub} = \frac{\pi}{2}\left(D^2 - d^2\right) + \pi d L \tag{19}$$

On introducing the aspect ratio, $\eta = \frac{L}{D}$, where $D = d_0 + 2W_0$, Eq. (19) becomes

$$A_{ub} = \pi\left[2W^2 + \eta d^2 + 2(1+\eta)Wd\right] \tag{20}$$

Using parts of Eq. (5), the above equation is further simplified as

$$A_{ub}(t_\varepsilon) = A_0 - \pi\left[B_1 \dot{r} t_\varepsilon + B_2 \dot{r}^2 t_\varepsilon^2 + B_3 \dot{r}^3 t_\varepsilon^3\right] \tag{21}$$

where t_ε is the instantaneous burning time.

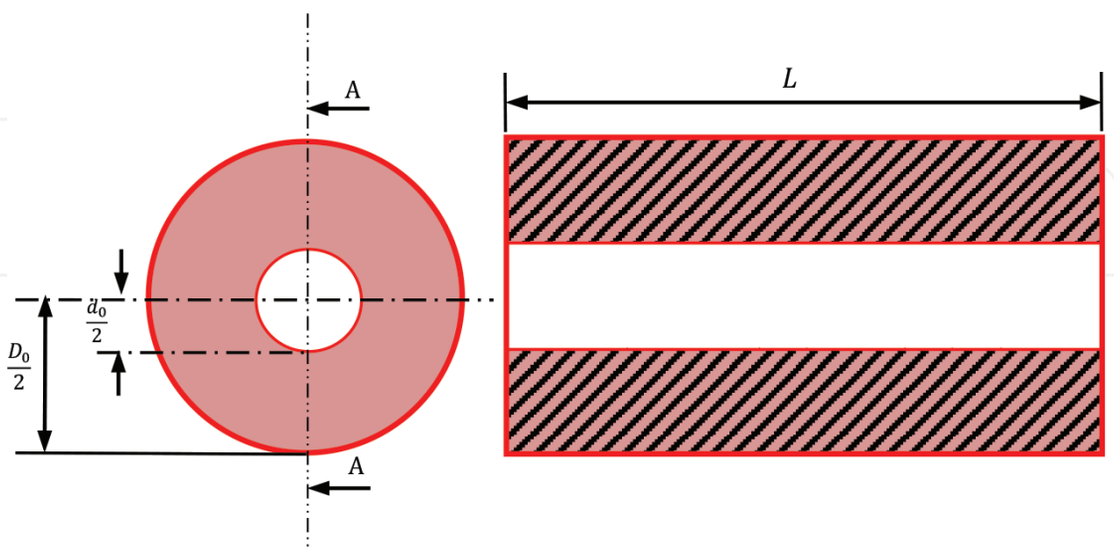

Figure 5. Tubular solid fuel geometrical parameters.

$$A_0 = \pi\left[2W_0^2 + 2(1+\eta_0)W_0 d_0 + \eta d_0^2\right]; \eta_0 = \frac{L_0}{d_0 + 2W_0};$$

$$B_1 = d_0\left[\frac{1}{\left(1+\frac{2W_0}{d_0}\right)} - 4\eta_0\right] + 2(1+\eta_0)(d_0 - W_0) + \frac{W_0}{\left(1+\frac{2W_0}{d_0}\right)}$$

$$B_2 = 2\left[(1-\eta_0) + \frac{2}{\left(1+\frac{2W_0}{d_0}\right)}\right]; B_3 = \frac{2}{\left(1+\frac{2W_0}{d_0}\right)}$$

Eq. (21) can be further written as

$$A_{ub}(t_\varepsilon) = A_{ub}(0) - A_b(t_\varepsilon) \tag{22}$$

where $A_{ub}(0) = A_0$, as illustrated below (**Figure 6**).

Above is the closed form expression for the instantaneous burning propellant area. Using Eq. (12), the kernel in the unburnt area $A_{ub}(t_\varepsilon)$ are rearranged to effect erosive regressive burning process, where

$$A_{ub}(t_\varepsilon) = A_0\left[1 - C_1\dot{r}t_\varepsilon - C_2\dot{r}^2t_\varepsilon^2 - C_3\dot{r}^3t_\varepsilon^3\right] \tag{23}$$

where $C_1 = \frac{B_1}{\Lambda_0}; C_2 = \frac{B_2}{\Lambda_0}; C_3 = \frac{B_3}{\Lambda_0}; \Lambda_0 = \left[2W_0^2 + 2(1+\eta_0)W_0 d_0 + \eta d_0^2\right]$

$$\Psi = \left[[(1+2\eta)W_0 + \eta d_0] + \left(\frac{2(W_0+d_0)\overline{\theta}_0}{4\eta\left(1+\frac{W_0}{d_0}\right) - \frac{\overline{\theta}_0 d_0}{W_0}}\right)\right]; \forall\ \ 0 \le \overline{\theta}_0 \le 2\pi.$$

By introducing $X_0 = \frac{W_0}{d_0}$, Eq. (23) results to

$$A_{ub}(t_\varepsilon) = \overline{A}_0\left[1 - \overline{C}_1\tau - \overline{C}_2\tau^2 - \overline{C}_3\tau^3\right] \tag{24}$$

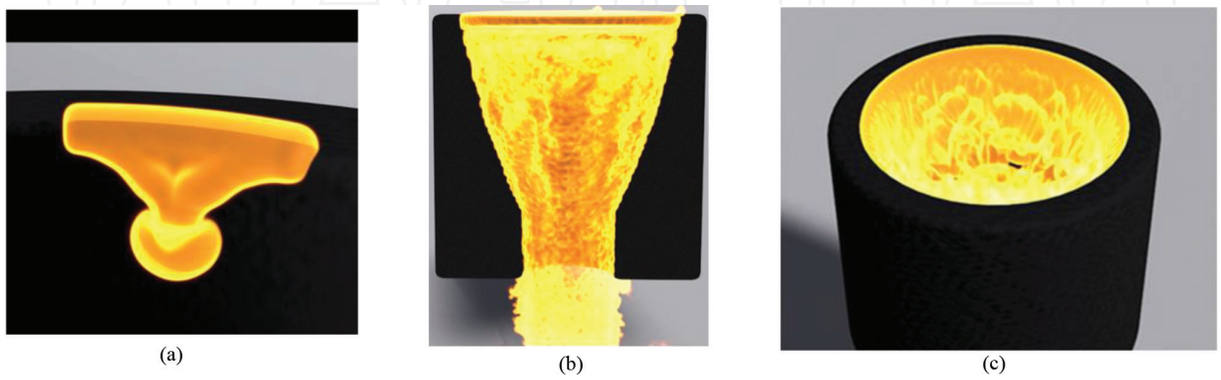

(a) (b) (c)

Figure 6. (a) Illustration of a point ignition at the commencement of burning propagation. (b) Cross section of burning propagation. (c) Complete burning process.

http://dx.doi.org/10.5772/intechopen.82822

where $\overline{A}_0 = \pi d_0^2\left[2\chi_0^2 + 2(1+\eta_0)\chi_0 + \eta_0\right]; \overline{C}_1 = \frac{\overline{B}_1\overline{\overline{\Psi}}}{\Lambda_0}; \overline{C}_2 = \frac{\overline{B}_2\overline{\overline{\Psi}}^2}{\Lambda_0}; \overline{C}_3 = \frac{\overline{B}_3\overline{\overline{\Psi}}^3}{\Lambda_0}$

where $\Lambda_0 = 2W_0^2 + 2(1+\eta_0)W_0 d_0 + \eta d_0^2; \overline{\overline{\Psi}} = [(1+2\eta)\chi_0 + \eta] + \left(\frac{\pi(1+\chi_0)}{\eta(1+\chi_0)-\frac{\pi}{2\chi_0}}\right)$

$$\text{Now at } t_\varepsilon = t_b \quad ; \quad A_{ub}(t_b) = A_0(1 - C_1 - C_2 - C_3) \tag{25}$$

From Eqs. (24) and (25), the non-dimensionalized unburnt propellant grain area is evaluated as

$$\frac{A_{ub}(t_\varepsilon)}{A_{ub}(t_b)} = A_{ub}(\tau) = \frac{\left[1 - \overline{C}_1\tau - \overline{C}_2\tau^2 - \overline{C}_3\tau^3\right]}{\left[1 - \overline{C}_1 - \overline{C}_2 - \overline{C}_3\right]} \tag{26}$$

Next, we return to the instantaneous burning area propagation via the following expression, namely:

$$A_b(t_\varepsilon) = \overline{A}_0\left[\overline{C}_1\tau + \overline{C}_2\tau^2 + \overline{C}_3\tau^3\right] \quad \forall \quad \tau = \frac{t_\varepsilon}{t_b} \tag{27}$$

$$\text{Now at } \; t_\varepsilon = t_b, A_b(t_b) = \overline{A}_0\left[\overline{C}_1 + \overline{C}_2 + \overline{C}_3\right] \tag{28}$$

From Eqs. (25) and (28), the non-dimensionalized form of the instantaneous burning area becomes

$$\frac{A_b(t_\varepsilon)}{A_b(t_b)} = \overline{A}_b(\tau) = \left(\frac{\overline{C}_1}{\overline{C}_1 + \overline{C}_2 + \overline{C}_3}\right)\tau + \left(\frac{\overline{C}_2}{\overline{C}_1 + \overline{C}_2 + \overline{C}_3}\right)\tau^2 + \left(\frac{\overline{C}_3}{\overline{C}_1 + \overline{C}_2 + \overline{C}_3}\right)\tau^3 \tag{29}$$

3.1. Effect of multiple ignition points

The effect of multiple ignition points (N_p) is expected to fractionalize the unburnt area time-dependent equations as follows, viz.:

$$A_{ub}(\tau) = \left(\frac{\frac{1}{N_p} - \overline{\overline{C}}_1\tau - \overline{\overline{C}}_2\tau^2 - \overline{\overline{C}}_3\tau^3}{\left(\frac{1}{N_p} - \overline{\overline{C}}_1 - \overline{\overline{C}}_2 - \overline{\overline{C}}_3\right)}\right); \forall\, \overline{\overline{C}}_1 = \overline{C}_1(N_p); \overline{\overline{C}}_2 = \overline{C}_2(N_p); \overline{\overline{C}}_3 = \overline{C}_3(N_p) \tag{30}$$

$$\overline{C}_1(N_p) = B_1\overline{\overline{\Psi}}(N_p); \overline{C}_2(N_p) = B_2\overline{\overline{\Psi}}^2(N_p); \overline{C}_3(N_p) = B_3\overline{\overline{\Psi}}^3(N_p)$$

$$\overline{\overline{\Psi}}(N_p) = \left[\left[\frac{(1+2\eta_0)\chi_0}{N_p} + \frac{\eta_0}{N_p}\right] + \left(\frac{\frac{\pi(1+\chi_0)}{N_p^2}}{\eta_0\left(\frac{1+\chi_0}{N_p}\right) - \frac{\pi}{2\chi_0 N_p^2}}\right)\right];$$

while for the burning area, the modification is

$$A_b(\tau) = \left(\frac{\overline{\overline{C}}_1\tau + \overline{\overline{C}}_2\tau^2 + \overline{\overline{C}}_3\tau^3}{\left(\overline{\overline{C}}_1 + \overline{\overline{C}}_2 + \overline{\overline{C}}_3\right)}\right) = \overline{\overline{B}}_1\tau + \overline{\overline{B}}_2\tau^2 + \overline{\overline{B}}_3\tau^3 \tag{31}$$

where

$$\overline{\overline{B}}_1 = \left[\frac{1}{1+2\chi_0} - 4\eta_0 + 2(1+\eta_0)(1-\chi_0) + \frac{\chi_0}{1+2\chi_0}\right]\overline{\overline{\Psi}};$$

$$\overline{\overline{B}}_2 = 2\left[(1-\eta_0) + \frac{2}{1+2\chi_0}\right]\overline{\overline{\Psi}}^2; \quad \overline{\overline{B}}_3 = \frac{2}{1+2\chi_0}\overline{\overline{\Psi}}^3$$

For $\chi_0 = \frac{W_0}{d_0} \ll 1$, Eqs. (26) and (31) can be further written as

$$A_{ub}(\tau) = \left(\frac{1 - \overline{\overline{C}}_1\tau - \overline{\overline{C}}_2\tau^2 - \overline{\overline{C}}_3\tau^3}{1 - \overline{\overline{C}}_1 - \overline{\overline{C}}_2 - \overline{\overline{C}}_3}\right); \ \forall \ \overline{\overline{C}}_1 = \frac{\overline{\overline{B}}_1\overline{\overline{\Psi}}}{\Lambda_0}; \ \overline{\overline{C}}_2 = \frac{\overline{\overline{B}}_1\overline{\overline{\Psi}}^2}{\Lambda_0}; \ \overline{\overline{C}}_3 = \frac{\overline{\overline{B}}_3\overline{\overline{\Psi}}^3}{\Lambda_0} \tag{32}$$

$$\overline{\overline{B}}_1 \approx 3(1-2\eta_0) - (3+2\eta_0)\chi_0 - 2{\chi_0}^2 \, ; \overline{\overline{B}}_2 \approx 2(3-\eta_0-4\chi_0); \overline{\overline{B}}_3 \approx 2(1-2\chi_0)$$

$$A_b(\tau) = \overline{\overline{B}}_1\tau + \overline{\overline{B}}_2\tau^2 + \overline{\overline{B}}_3\tau^3 \tag{33}$$

Note that these closed form propagation profiles are kinematically derived. From the kernels, they exhibit third-order polynomial equations. To enable us study these profiles further, the following ordinary differential equation (ODE) modeling follows in the subsection.

4. Ordinary differential equation (ODE) modeling

As previously done, the modeling is taking off from the unburnt propagation problem. Given that $A_{ub}(t_\varepsilon)$ and $A_{ub}(t_\varepsilon + \Delta t_\varepsilon)$ are unburnt propellant grains at time (t_ε) and $(t_\varepsilon + \Delta t_\varepsilon)$, respectively, it is apparent that $A_{ub}(t_\varepsilon + \Delta t_\varepsilon) < A_{ub}(t_\varepsilon)$; $\forall\ 0 < t_\varepsilon < (t_\varepsilon + \Delta t_\varepsilon)$.

Consequently,

$$\lim_{\Delta t_\varepsilon \to 0}\left(\frac{A_{ub}(t_\varepsilon + \Delta t_\varepsilon) - A_{ub}(t_\varepsilon)}{\Delta t_\varepsilon}\right) = \frac{-dA_{ub}(t)}{dt_\varepsilon} \tag{34}$$

leading to a simple linear ODE of the form

$$\frac{dA_{ub}(t_\varepsilon)}{dt_\varepsilon} = -\lambda_b A_{ub}(t_\varepsilon) \tag{35}$$

where $\lambda_b =$ propagation constant/s.

For Eq. (35) to be well posed, the following conditions are specified, viz.:

$$(i) \quad t_\varepsilon = 0; \ A_{ub}(0) = A_0$$

$$(ii) \quad t_\varepsilon = t_b; \ A_{ub}(t_b) = -A_0(C_1 + C_2 + C_3) \ \forall \ A_{ub}(t_b) + A_b(t_b) = 0 \tag{36}$$

http://dx.doi.org/10.5772/intechopen.82822

In the meantime, the solution to Eq. (35) is given by

$$\therefore A_{ub}(t_\varepsilon) = A_{ub}(0)e^{-\lambda_b t_\varepsilon} \tag{37}$$

On imposing the conditions in Eq. (36), the following closed forms ensue, namely:

$$\therefore A_{ub}(t_\varepsilon) = A_{ub}(0)e^{-\lambda_b t_\varepsilon} \tag{38}$$

$$A_{ub}(t_\varepsilon) = A_0 e^{-\lambda_b t_\varepsilon} = A_0(C_1 + C_2) \tag{39}$$

Meanwhile, Eq. (38) satisfies the following form:

$$A_{ub}(t_\varepsilon) = A_0 e^{-\beta}\left(\frac{t_\varepsilon}{t_b}\right) = A_0 e^{-\beta\tau};\ \forall\ \beta = \ln\left(C_1 + C_2 + C_3\right);\ \tau = \frac{t_\varepsilon}{t_b} \tag{40}$$

to give a simple relation of the form

$$\overline{A}_{ub}(\tau) = e^{\beta(1-\tau)}\ \forall\ \beta = \ln\left(\overline{C}_1 + \overline{C}_2 + \overline{C}_3\right) \tag{41}$$

The foregoing represents the generalized unburnt propellant area propagation as a function of the dimensionless time(τ). To enable us generate semi-infinite polynomial models, the following series approximation suffices, namely:

$$\begin{aligned} e^{\beta(1-\tau)} &\approx \sum_{n=0}^{\infty}\frac{\beta^n(1-\tau)^n}{n!} \\ &\approx \left\{1 + \beta(1-\tau) + \frac{\beta^2(1-\tau)^2}{2!} + \frac{\beta^3(1-\tau)^3}{3!} + \frac{\beta^4(1-\tau)^4}{4!} + \ldots + \frac{\beta^n(1-\tau)^n}{n!} + R_N(\beta,\tau)\right\} \end{aligned} \tag{42}$$

From Eqs. (43) and (44), linear to infinite order profiles can be further deduced. A few illustrations follow, namely:

a. Linear unburnt area profile

$$A_{ub}^{(1)}(\tau) = \left((1+\beta) - \beta\tau\right) \tag{43}$$

b. Secondary degree unburnt area propagation profile (quadratic)

$$A_{ub}^{(2)}(\tau) = \left(\left(1 + \beta + \frac{\beta^2}{2}\right) - \left(\beta + \beta^2\right)\tau + \frac{\beta^2}{2}\tau^2\right) \tag{44}$$

c. Third-degree unburnt area propagation profile (cubic)

$$A_{ub}^{(3)}(\tau) = \left(\left(1 + \beta + \frac{\beta^2}{2} + \frac{\beta^3}{6}\right) - \left(\beta + \beta^2 + \frac{\beta^3}{2}\right)\tau + \left(\frac{\beta^2 + \beta^3}{2}\right)\tau^2 - \frac{\beta^3}{6}\tau^3\right) \tag{45}$$

d. Fourth-degree unburnt area propagation profile

$$A_{ub}^{(4)}(\tau) = \left(\left(1+\beta+\frac{\beta^2}{2}+\frac{\beta^3}{6}+\frac{\beta^4}{24}\right) - \left(\beta+\beta^2+\frac{\beta^3}{2}-\frac{2\beta^4}{3}\right)\tau + \left(\frac{\beta^2+\beta^3}{2}+\frac{\beta^4}{4}\right)\tau^2 - \left(\frac{\beta^3}{6}+\frac{\beta^4}{6}\right)\tau^3 + \left(\frac{\beta^4}{24}\right)\tau^4\right) \tag{46}$$

e. Nth degree unburnt area propagation profile

$$A_{ub}^{(Nth)}(\tau) = \left\{1+\beta(1-\tau)+\frac{\beta^2(1-\tau)^2}{2!}+\frac{\beta^3(1-\tau)^3}{3!}+\frac{\beta^4(1-\tau)^4}{4!}+\ldots+\frac{\beta^N(1-\tau)^N}{N!}\right\} \tag{47}$$

4.1. Burning propellant area modeling

The burning area $A_b(t_\varepsilon)$ can be deduced from the following equation, namely:

$$A_b(t_\varepsilon) = A_{ub}(0) - A_{ub}(t_\varepsilon) \tag{48}$$

resulting to an expression of the form

$$A_b(t_\varepsilon) = A_0\left(1-e^{-\lambda_b t_\varepsilon}\right) \tag{49}$$

subject to the following conditions, viz.:

$$\begin{aligned} &(i) \quad t_\varepsilon = 0; A_b(t_\varepsilon) = 0 \\ &(ii) \quad t_\varepsilon = t_b; A_b(t_b) = \overline{A}_0\left(\overline{C}_1+\overline{C}_2+\overline{C}_3\right) \end{aligned} \tag{50}$$

Note that Eq. (47) from the second part of Eq. (48) becomes

$$A_b(t_b) = A_0\left(1-e^{-\beta\left(\frac{t_\varepsilon}{t_b}\right)}\right) \tag{51}$$

such that at

$$t_\varepsilon = t_b; A_b(t_b) = A_0\left(1-e^{-\beta}\right) \tag{52}$$

from which the following equation ensues:

$$\frac{A_b(t_\varepsilon)}{A_b(t_b)} = \overline{A}_b(\tau) = \left(\frac{1-e^{-\beta\tau}}{1-e^{-\beta}}\right) \tag{53}$$

upon using the following series approximations, viz.:

http://dx.doi.org/10.5772/intechopen.82822

$$e^{-\beta\tau} \approx \sum_{n=0}^{\infty} \frac{(-\beta\tau)^n}{n!} \quad ; \quad e^{-\beta\tau} \approx \sum_{n=0}^{\infty} \frac{(-\beta)^n}{n!} \tag{54}$$

The following hold, namely:

$$\left(1 - e^{-\beta\tau}\right) \approx \left(1 - \sum_{n=0}^{\infty} \frac{(-\beta\tau)^n}{n!}\right); \quad \left(1 - e^{-\beta}\right) \approx \left(1 - \sum_{n=0}^{\infty} \frac{(-\beta)^n}{n!}\right) \tag{55}$$

The use of the above equations transforms $\overline{A}_b(\tau)$ as

$$\overline{A}_b(\tau) = \frac{\sum_{N=0}^{\infty} \frac{(-1)^{N+1}\beta^N\tau^N}{N!}}{\sum_{N=1}^{\infty} \frac{(-1)^{N+1}\beta^N}{N!}} \tag{56}$$

The following approximated profiles can be generated, viz.:

(a) First-degree profile (linear)

$$\overline{A}_b^{(1)}(\tau) = \frac{\beta\tau}{\sum_{N=1}^{\infty} \frac{(-1)^{N+1}\beta^N}{N!}}$$

(b) Second-degree profile (quadratic)

$$\overline{A}_b^{(2)}(\tau) = \frac{\sum_{N=1}^{2} \frac{(-1)^{N+1}\beta^N\tau^N}{N!}}{\sum_{N=1}^{\infty} \frac{(-1)^{N+1}\beta^N}{N!}}$$

(c) Third-degree profile (cubic)

$$\overline{A}_b^{(3)}(\tau) = \frac{\sum_{N=1}^{3} \frac{(-1)^{N+1}\beta^N\tau^N}{N!}}{\sum_{N=1}^{\infty} \frac{(-1)^{N+1}\beta^N}{N!}}$$

(d) Fourth-degree profile (biquadratic)

$$\overline{A}_b^{(4)}(\tau) = \frac{\sum_{N=1}^{4} \frac{(-1)^{N+1}\beta^N\tau^N}{N!}}{\sum_{N=1}^{\infty} \frac{(-1)^{N+1}\beta^N}{N!}}$$

(e) Mth order degree profile

$$\overline{A}_b^{(M)}(\tau) = \frac{\sum_{N=1}^{M} \frac{(-1)^{N+1}\beta^N\tau^N}{N!}}{\sum_{N=1}^{\infty} \frac{(-1)^{N+1}\beta^N}{N!}} \tag{57}$$

5. Effect of multiple ignition points

The effects of multiple ignition points are accounted for in the following equations, viz. (unburnt area propagation):

$$\overline{A}_{ub}^{(N_p)}(\tau) = e^{\beta(N_p)(1-\tau)}; \overline{A}_b^{(N_p)}(\tau) = \left(\frac{1 - e^{-\beta(N_p)\tau}}{1 - e^{-\beta(N_p)}}\right) \tag{58}$$

where $\beta(N_p) = \ln\left(\overline{C}_1(N_p) + \overline{C}_2(N_p) + \overline{C}_3(N_p)\right)$

For the various associated polynomials, the matching kernel $\alpha(N_p)$ applies.

6. Discussion of results

Having shown the details of mathematical analyses, which leads to the derivation of closed form equations for both burning and unburnt propellant grain areas, subject to treating a flame particle arising from one to multiple ignition points theoretically using Newtonian mechanics, we shall now shift focus to discussing parametric modulations of these closed form equations. The interest here is to match theoretical simulated burn time results to those of conducted static burning tests of the propellant as demonstrated in **Figures 7** and **8**. Firstly, a cache of experimental set-ups for measuring the burn time are illustrated in **Figures 7** and **8**.

The static test rig holder as shown in **Figures 7** and **8** has an in-built sensor system which captures the burning propagation signature in the form of a digitized time signal that is fed into a transducer for a real-time display. A redundant system that has a stop-watch is also utilized for comparative purposes. After a number of static test experiments as demonstrated in **Figures 7** and **8**, the experimental results and theoretical comparisons are contained in **Tables 2** and **3**. The parameters of the solid propellant and combustion chamber are highlighted in **Tables 1** and **4**.

Meanwhile, the associated generalized chemical combustion equation for two classical composite formulations as illustrated below, namely,

Dextrose-based composite combustion equation:

$$6.09KNO_{3(s)} + 1.438C_6H_{12}O_{6(s)} + 4.11M_{g(s)} + 1.07C_{(s)} + 0.094Fe_2O_{3(s)} = 5.17CO_{(g)} + 4.94KOH_{(g)} + 4.74H_2O_{(g)} + 4.11CO_{2(g)} + 4.11MgO_{(s)} + 3.12N_{2(g)} + 1.42H_{2(g)} + 1.15K_{(g)}$$

Figure 7. Static test rigs with single motor.

http://dx.doi.org/10.5772/intechopen.82822

Figure 8. Static test rigs with tri-cluster rocket motors.

Mass of propellant (kg)	Web thickness w_0 (m)	Internal diameter d_0 (m)	Outer diameter D (m)	Total length of grain L (m)	Aspect ratio (η)	Chamber pressure (MPa)
4.26	0.0360	0.0380	0.110	0.277	2.518	5.676
4.59	0.0276	0.0497	0.105	0.373	3.547	8.160
5.19	0.0360	0.0380	0.110	0.338	3.070	7.133
5.97	0.0276	0.0497	0.105	0.521	4.914	10.715

Table 1. Experimental parameters.

Sorbitol-based composite combustion equation:

$$5.53KNO_{3(s)} + 1.42C_6H_{14}O_{6(s)} + 4.11M_{g(s)} + 0.378C_{(s)} + 0.377Fe_2O_{3(s)} = 5.59CO_{(g)} + 5.44H_2O_{(g)} + 4.48KOH_{(g)} + 4.11MgO_{(s)} + 3.32CO_{2(g)} + 3.12N_{2(g)} + 2.28H_{2(g)} + 1.05K_{(g)}$$

Figure 9 depicts the behavioral pattern of the burn time as a function of the burn rate in conjunction with the modulating role of number of ignition points. It is noted from the closed form expression Eq. (16) that an inverse or semi-hyperbolic relationship holds for each of the curves asymptotically. From design consideration, ab initio prediction can be conjured for appropriate ballistic suitability (**Tables 2–4**). Secondly, reduction in burn time is noted with higher ignition points for any burn rate, by having a hold on other variables as couched in Eq. (16). Very significantly, the role of the ignition points is essential for controlling the amount of transient buildup of the combustion chamber pressure in such a manner that is helpful to fasten the occurrences of explosion if hollow cylindrical explosives are desired for military purposes. This transient pressure can be built up very rapidly and reach high levels for a very

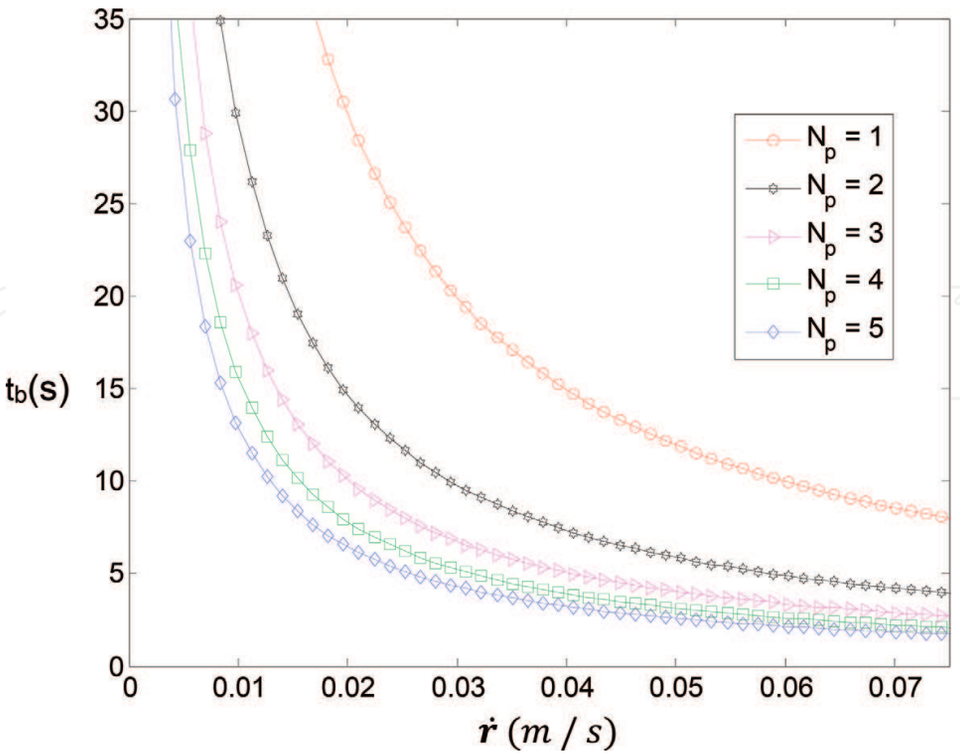

Figure 9. Plot of burn time against regression rate.

Mass of propellant (kg)	Theoretical burn time t_b (s) ($\theta = \pi$)	Theoretical burn time t_b (s) ($\theta = 2\pi$)	Experimental result burn time $t_a = t_b + t_s$ (s)
4.26	4.640	4.757	5.27
4.59	5.899	6.023	6.13
5.19	5.507	5.595	7.00
5.97	7.943	8.032	8.00

t_b, total burn time calculated; t_a, experimental burn time result; t_s, burnout time; θ, total sectorial angle covered by flame.

Table 2. Experimental results.

short burn time. It is very important to state here that such pressure value preferences must take into cognizance of the ultimate tensile strength of the combustion chamber material to forestall thermal rupturing of the walls.

In the meantime, **Figure 10** indicates the characteristic profiles of the burn time as a function of web thickness to core diameter ratio. As seen clearly, two zones are exhibited with a jump tendency in each case. Notably too, the effect of multiple ignition points is copiously observed to be very central here. As an option, a preferred burn time to govern the fuel ballistic characteristics can be selected to match desired ignition points by holding other parametric values of the grain geometry. Meanwhile, in the first zone, the burn time is noted to be fairly constant before transiting through an impulsive spark to a local peak. Beyond these points,

http://dx.doi.org/10.5772/intechopen.82822

Mass of propellant (kg)	Theoretical burn time t_b (s) ($\theta = \pi$)	Theoretical burn time t_b (s) ($\theta = 2\pi$)	Experimental result burn time t_a(s)
4.26	4.640	4.757	5.27
4.59	5.899	6.023	6.13
5.19	5.507	5.595	7.00
5.97	7.943	8.032	8.00

Table 3. Experimental results (burn time).

First set		Second set	
L (m)	0.521	L (m)	0.528
D (m)	0.105	D (m)	0.105
d_0 (m)	0.0497	d_0 (m)	0.038
$\dot{r}$ (m/s)	0.0688	$\dot{r}$ (m/s)	0.0688
a ($m^2kg^{-1}\ s^{-1}$)	0.01899		

Table 4. Table of simulation parameters.

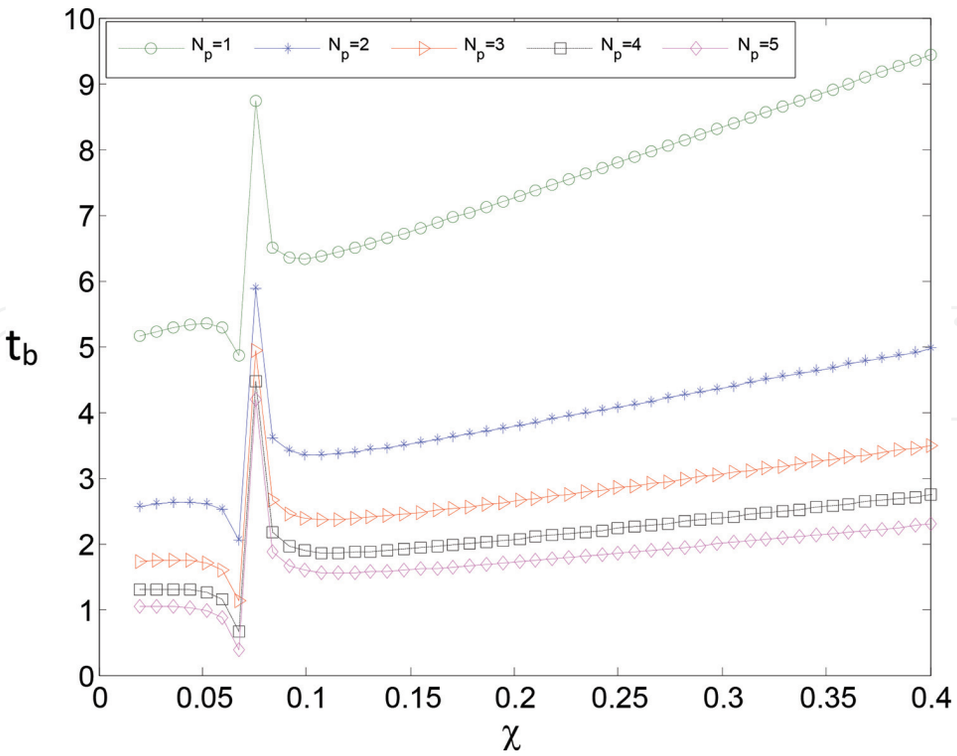

Figure 10. Plot of normalized burn time against χ.

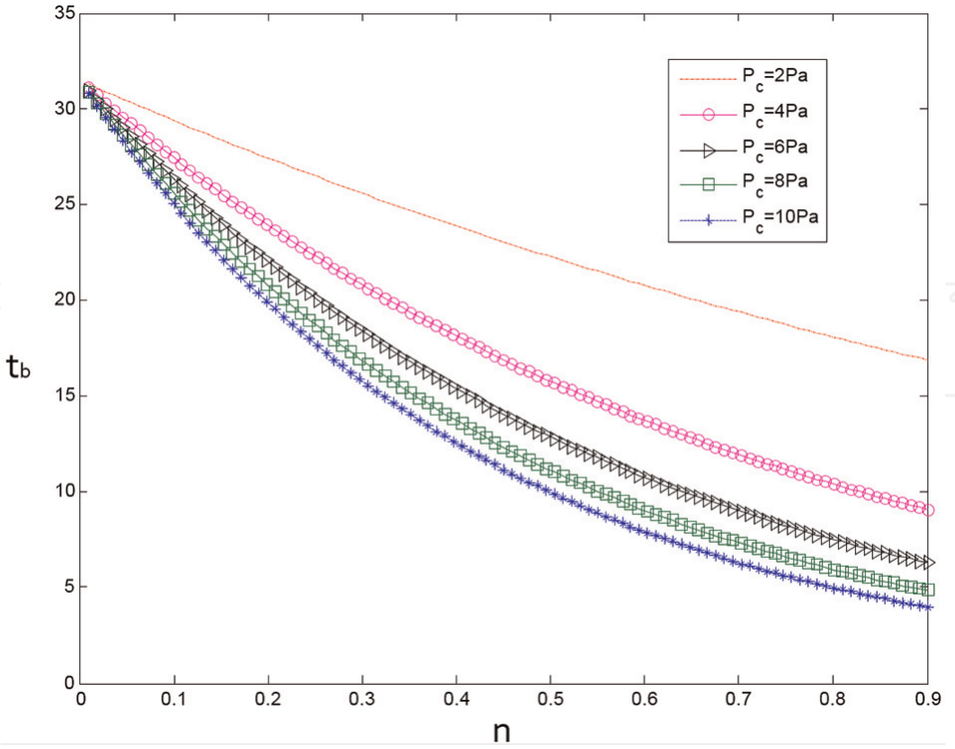

Figure 11. Plot of burn time against pressure index.

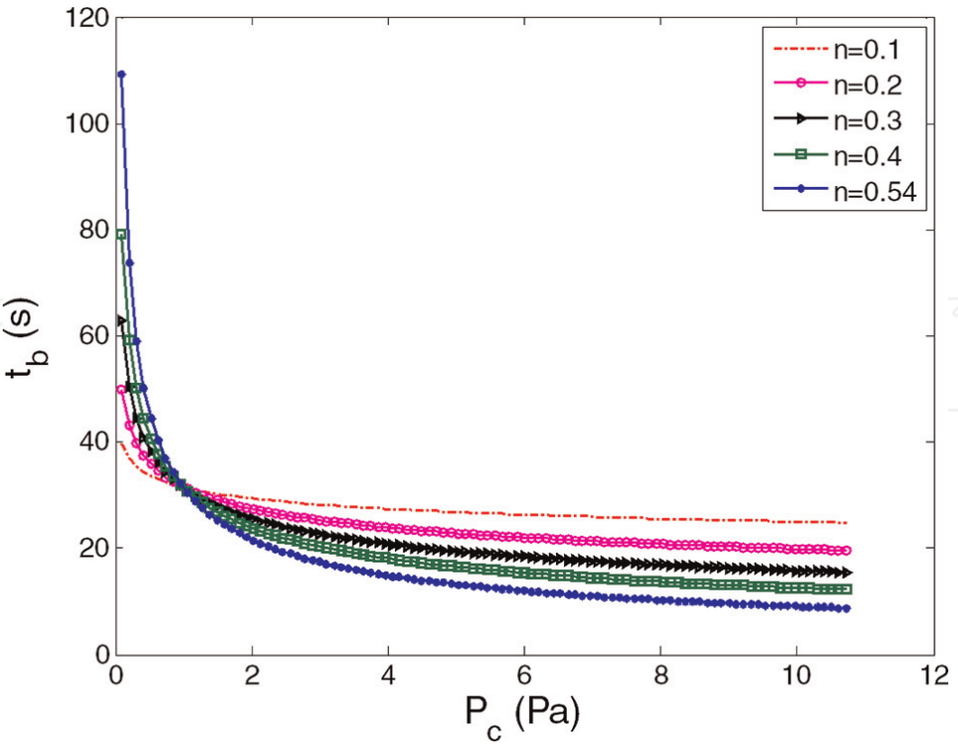

Figure 12. Plot of burn time against pressure.

http://dx.doi.org/10.5772/intechopen.82822

slight droppings are noted till sharp turning points are initiated to prompt monotonic increasing linear profiles.

In the meantime, we illustrate in **Figure 11** the characteristics of the burn time versus the propellant characterization index. Expectedly, all the curves originate from a common point irrespective of the value or quantum of the combustion chamber pressure. It is a direct consequence of Saint Robert Veille's law adopted for this study. In general, inverse relationships for any kernels must hold as can be inferred from the nature of the closed form equation tying the burn time with other parametric values deducible from empirical relations as published in literature.

Figure 12 illustrates the plot of burn time against combustion chamber pressure for any index (n). Here, we note two zones in each case where increasing pressure has decreasing effects on the burn time consistently up to a common crossover point before exhibiting reverse ordering to prompt fairly constant horizontal curves for any index value. Parts of these characteristics are previously noted in **Figure 11**. We expect these profiles to be generic irrespective of the propellant formulation and chemistry for this class of solid geometry. In grain design exercise, a number of choices are handy starting from index selection to consideration of stress tolerance of the chamber wall and aerothermodynamic properties arising from a fuel compositional chemistry and reaction kinetics.

Having examined the characteristic profiles of the burn time as modulated by specified parameters in the previous figures, we next shift focus in observing the commutative effects it is having on the burning and unburning propellant grain areas. Firstly, the behavioral pattern of

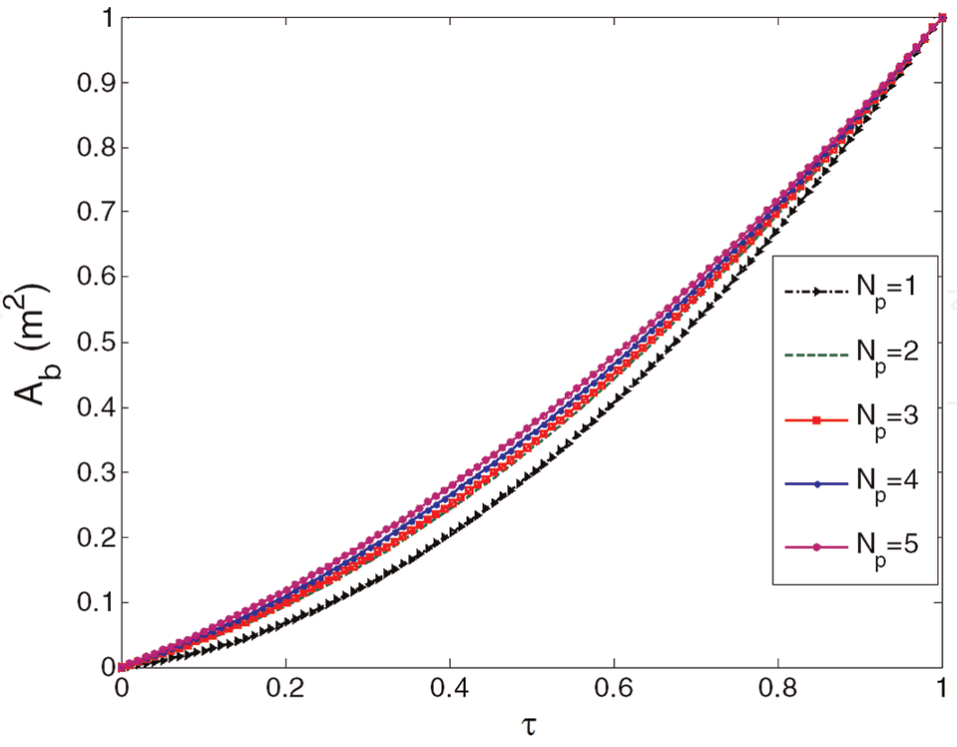

Figure 13. Plot of burnt area against normalized time.

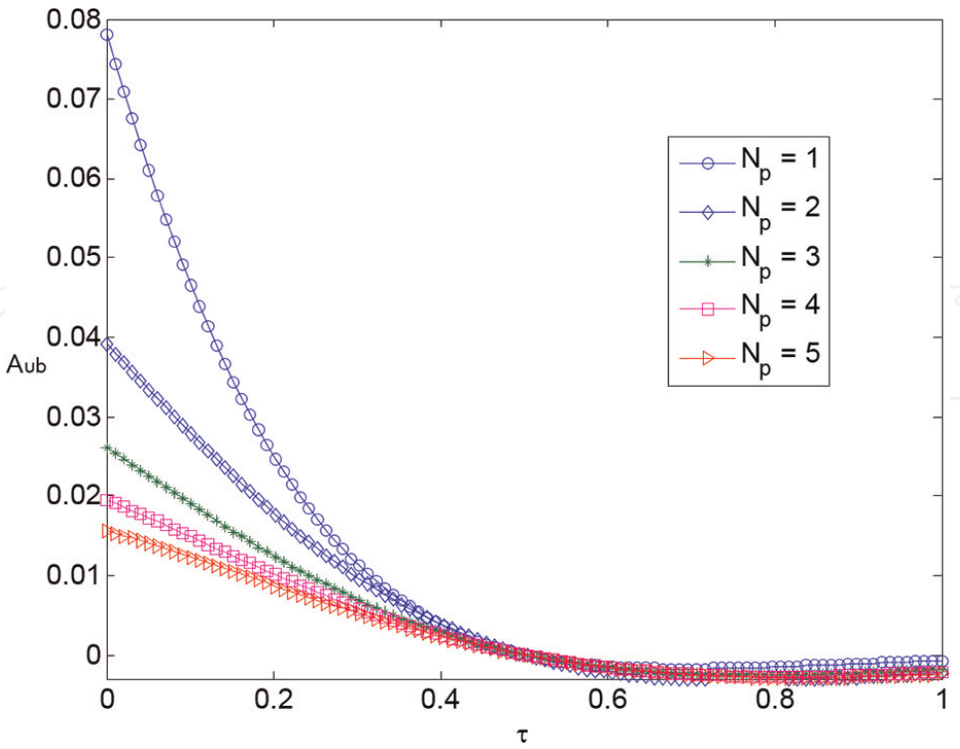

Figure 14. Plot of normalized unburnt area against normalized time.

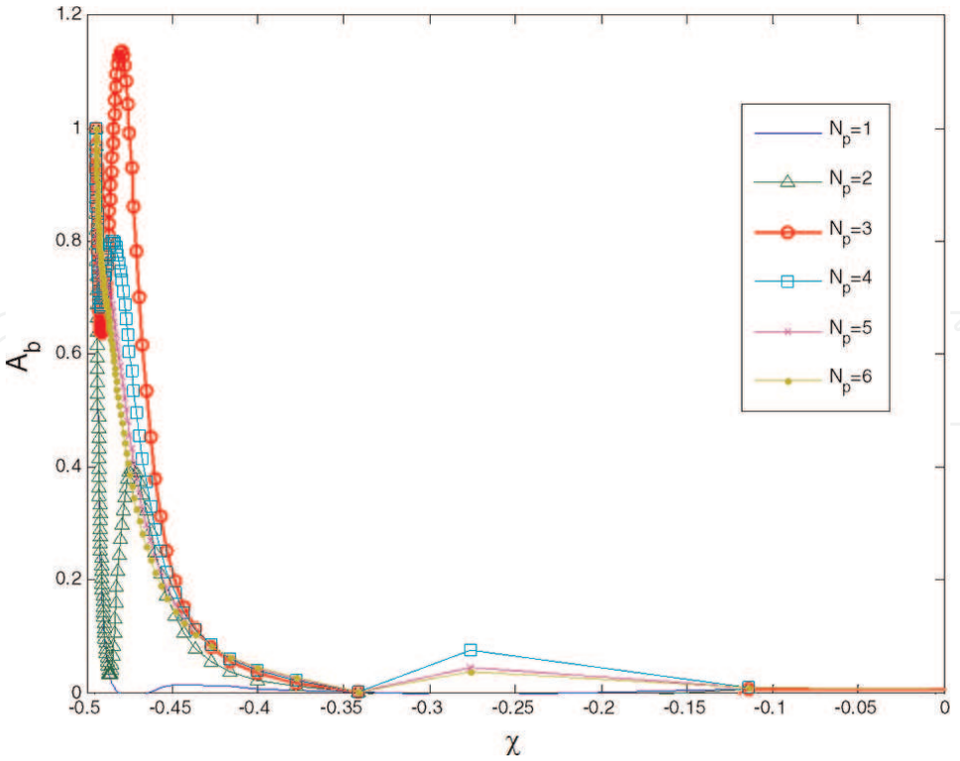

Figure 15. Plot of burnt area against χ.

http://dx.doi.org/10.5772/intechopen.82822

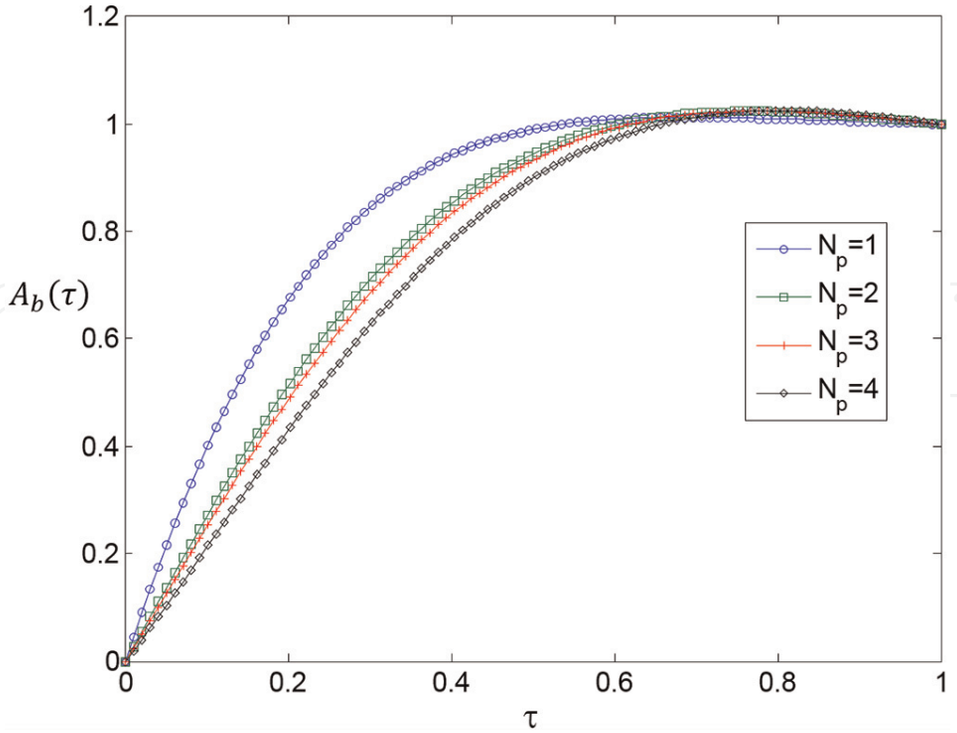

Figure 16. Plot of normalized burnt area against normalized time.

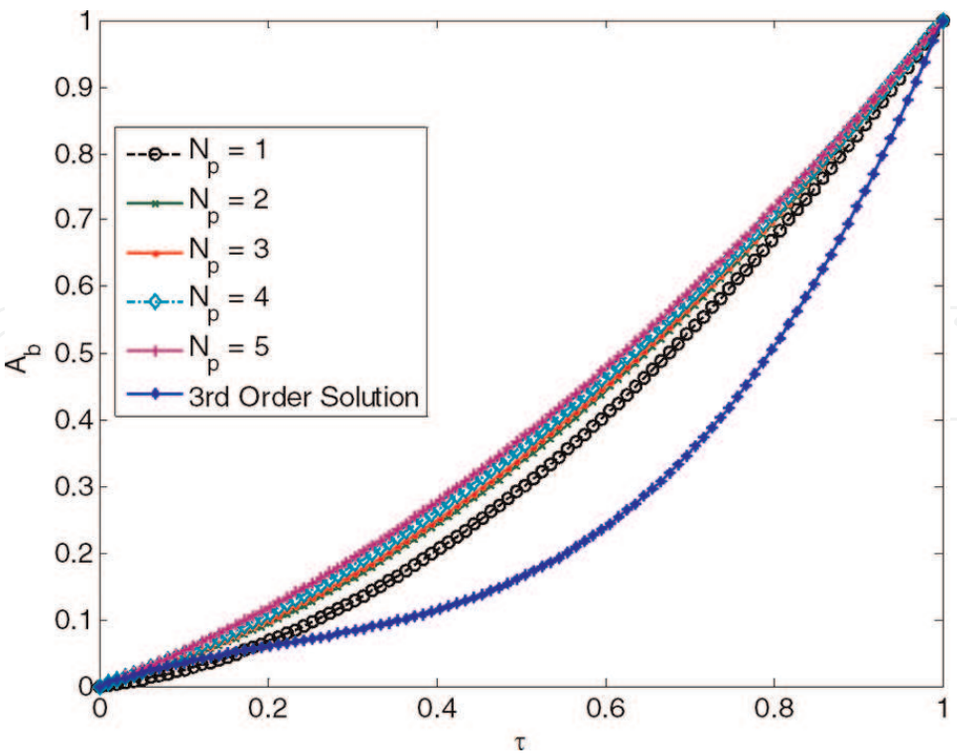

Figure 17. Comparison of a third-order polynomial approximation with kinematic prediction of burn area against time.

the burning area against the normalized burn time is illustrated in **Figure 13**. As can be seen, ordering is in consonance with increasing number of ignition points. Note clearly too that profiles are curvilinear for all the ignition points. We now proceed further to the case of the ordinary differential equation model in the illustration. Next, as seen, ordering is in reverse consonance with increasing number of ignition points. Note clearly that the pattern of profiles is curvilinear for all the ignition points. These distinct appearances are apparently visible from the onset, while overlapping tendencies are exhibited from the midpoint of the normalized time. This is possibly sequel to the segmental placement of the ignition points, to reduce the unburnt areas proportionally as indicated in the vertical axis of the plotted figure.

At this point, we shift focus to studying the ordinary differential equation model for predicting the behavioral pattern for a temporal dependent closed form unburnt grain depreciation conjectural result. The mathematical functional relation is a geometrically decaying exponential kernel that is tied to the parametric variables linking a number of factors ranging from the aspect ratio to the web thickness and the number of points at which the propellant bate is ignited. **Figure 14** depicts the behavioral pattern of the unburnt area as a function of normalized time in conjunction with the modulating role of ignition points. As can be seen, all the curves exhibit a decaying exponential characteristic. This is expected, as Eq. (41) is an exponential function. Next, as seen, ordering occurs in the order of increasing ignition points.

Figure 15 is a plot of Eq. (58) to demonstrate the modulating roles of web thickness to core diameter ratio (χ) on the burning area propagation for one to multiple (six) ignition points in

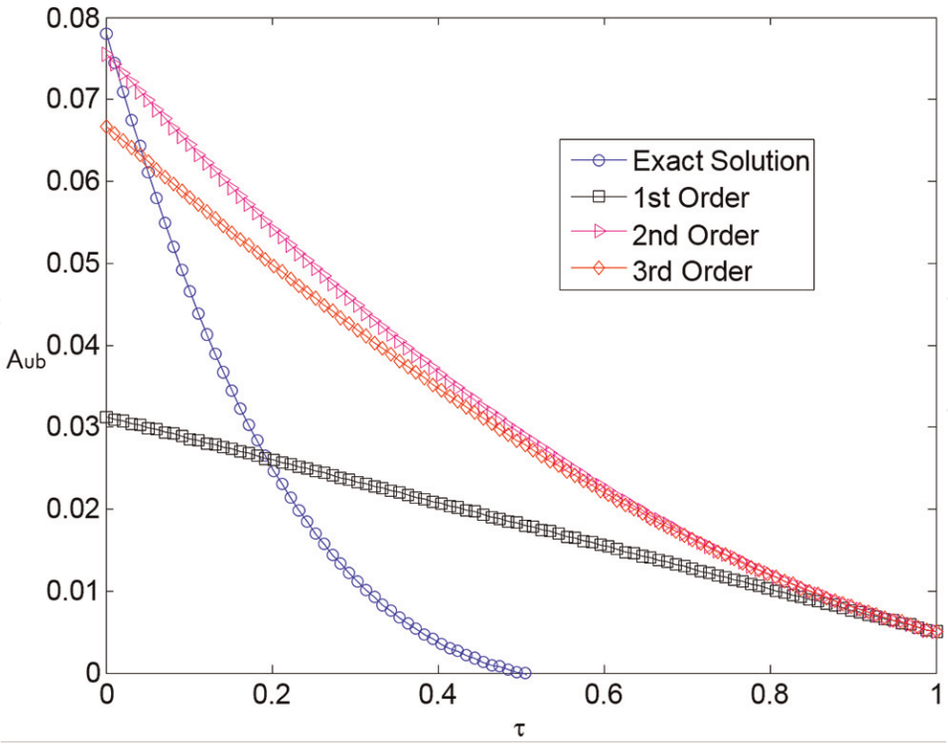

Figure 18. Plot of polynomial approximations of normalized unburnt area.

http://dx.doi.org/10.5772/intechopen.82822

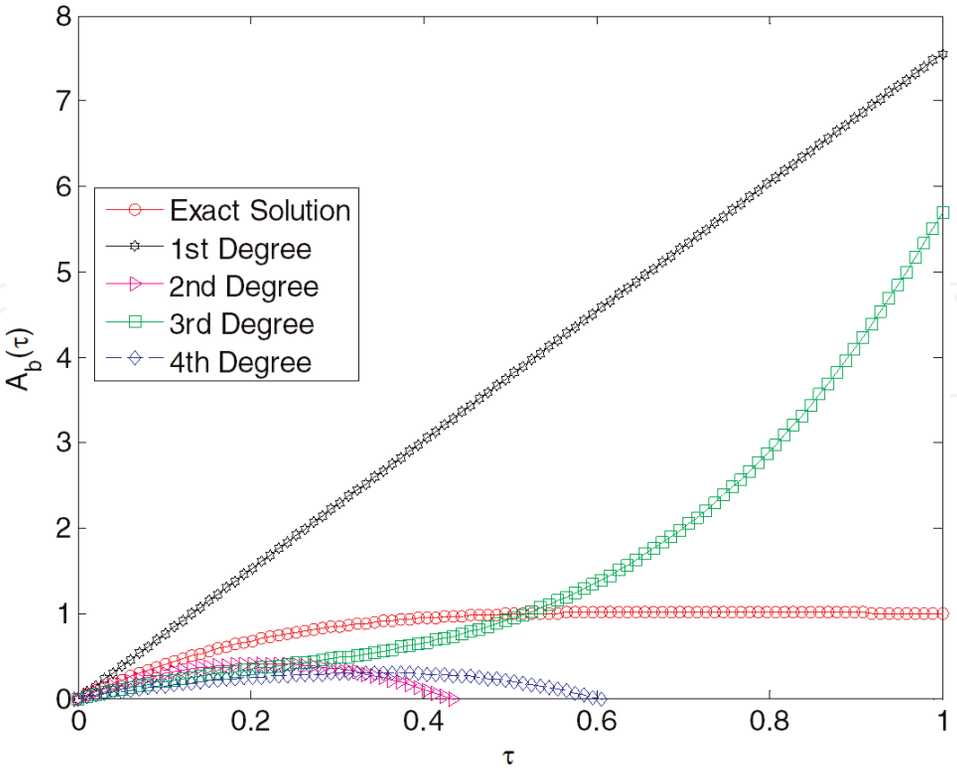

Figure 19. Plot of polynomial approximations of normalized burnt area: Eq. (54).

the range of χ hyperbolic profiles as noted for $N_p = 1$ and $N_p = 2$. A turning point is initiated at the maximum point and thereafter decreases asymptotically.

The profile of non-dimensionalized burnt area with respect to normalized time is depicted in **Figure 16**. Firstly, for the different numbers of ignition points simulated, the normalized burnt area has a characteristic increasing curvilinear signature. Secondly, the curves are ordered with increasing ignition points. There is also an overlap of the curves at the beginning and end points.

The kinematic prediction of burn area against time is illustrated in **Figure 17**. As can be seen, the profiles are curvilinear for all the points of ignition. With increasing number of ignition points, the curvilinear signature tends toward a linear profile. Next, as seen, ordering is in reverse consonance with increasing number of ignition points. Note clearly that the profiles are curvilinear for all the ignition points. These distinct appearances are apparently visible from the onset, while overlapping tendencies are exhibited from the midpoint of the normalized time. The third-order burnt area propagation profile also exhibits a curvilinear profile that is similar to the kinematic prediction.

The polynomial approximations of unburnt area propagation of the propellant are depicted in **Figure 18**. For all orders of the polynomial approximations, profiles are fairly linear with monotonic decreases. The exact solution on the other hand is a decreasing curvilinear profile with a steeper slope than the approximations. All the polynomial approximations have approximately equal values of unburnt area at onset of the time period and decrease to the

same value at the end of the burning. The value at the end of the period can be regarded as the unburnt propellant residue.

The profiles of first- to fourth-degree approximate burnt area propagation and the exact polynomial solution are shown in **Figure 19**. The exact solution manifests an initial increasing curvilinear feature for the first half of the burning period. During the second half of burning, the burnt area is constant until the end of the period. The second- and fourth-degree approximations have similar profiles. They rise to a maximum and fall curvilinearly to zero. The first-degree polynomial increases linearly throughout the period, while the third-degree approximation rises curvilinearly to a value above the exact solution.

7. Conclusion

This chapter proposes the derivation of equations to predict burn time, burning and unburnt area propagation of a tubular propellant grain. A regressive solid fuel pyrolysis in a cylindrical combustion chamber is assumed to hold. The behavioral patterns of simulated results reveal the modulating impact of variables on the burning propagation due to the kinematic and mathematical models. Closed form expressions are couched in terms of the propellant grain geometrical constraints. In addition, for the burn time, a close conformity between theoretical models and experimental results is shown.

Our findings include:

1. The reduction in burn time is noted with higher ignition points for any burn rate, by having a hold on other variables as couched in Eq. (16).
2. An inverse or semi-hyperbolic relationship holds for the relationship between burn time and the burn rate.
3. Increasing pressure has decreasing effects on the burn time consistently up to a common crossover point.
4. The profiles of burn area with time are curvilinear for all the points of ignition. With increasing number of ignition points, the curvilinear signature tends toward a linear profile.

The above find application in the use of variable number of ignition points for controlling the amount of transient buildup of the combustion chamber pressure. This helps to fasten the occurrences of explosion if hollow cylindrical explosives are desired for military purposes. Also, preferred burn time to govern the fuel ballistic characteristics can be selected to match desired ignition points by holding other parametric values of the grain geometry constant. In grain design exercise, different parameters can be altered, namely, pressure index selection to consideration of stress tolerance of the chamber wall and aerothermodynamic properties arising from a fuel compositional chemistry and reaction kinetics.

http://dx.doi.org/10.5772/intechopen.82822

Nomenclature

A	constant.
W	Web thickness of tubular propellant grain.
L	Length of tubular propellant grain.
A_s	Sectorial area of tubular propellant grain.
$\dot{r}$	Constant regression rate.
χ	Ratio of web thickness to diameter.
η	Aspect ratio; ratio of propellant bate length to diameter.
A_{ub}	Unburnt area.
A_b	Burnt area.
N_p	Number of ignition points.
λ_p	Propagation constant/sec.
P_c	Combustion chamber pressure.
n	Propellant characteristic index.

Author details

Charles A. Osheku[1,2*], Oluleke O. Babayomi[1] and Oluwaseyi T. Olawole[1]

*Address all correspondence to: charlesosheku2002@yahoo.com

1 Centre for Space Transport and Propulsion, National Space Research and Development Agency, Federal Ministry of Science and Technology, Lagos, Nigeria

2 Department of Systems Engineering, Faculty of Engineering, University of Lagos, Lagos, Nigeria

References

[1] Tseng IS, Yang V. Combustion of a double-base homogeneous propellant in a rocket motor. Combustion and Flame. 1994;**96**:325-342

[2] Roh TS, Tseng IS, Yang V. Effects of acoustic oscillations on flame dynamics of homogeneous propellants in rocket motors. Journal of Propulsion and Power. 1995;**11**:640

[3] Roh T-S, Apte SV, Yang V. Proceedings of the Combustion Institute. 1998;**27**:2335-2341

[4] Roh T-S, Yang V. AIAA Paper No. 96-2623

[5] Roh T-S, Apte SV, Yang V. Progress in Astronautics and Aeronautics. 2000;**185**:837-857

[6] Apte S, Yang V. Proceedings of the Combustion Institute. 2000;**28**:903-910

[7] Zmelter J, Ortiz P. Burning surfaces evolution in solid propellants: A numerical model. Proceedings of the Institution of Mechanical Engineers, Part G: Journal of Aerospace Engineering. **221**(3):429-439

[8] Atwood AI, Ford KP, Wheeler CJ. High pressure burning rate studies of solid rocket propellants. Progress in Propulsion Physics. 2013;**4**:3-14

[9] Favaró FM, Sirignano WA, Manzoni M, DeLuca LT. Solid-fuel regression rate modeling for hybrid rockets. Journal of Propulsion and Power. 2013;**29**(1)

[10] Krier H, Rajan S, Van Tassell WF. Flame-spreading and combustion in packed beds of propellant grains. AIAA Journal. 1976;**14**(3):301-309

[11] Jackson TL, Zhang J, Topalian V. Erosive burning of solid propellants. In: 48th AIAA Aerospace Sciences Meeting Including the New Horizons Forum and Aerospace Exposition; 4–7 January 2010; Orlando, Florida

[12] Kadosh JS. A general note on modeling approaches for solid rocket fuel burning. Green Lightning Research Paper SRM-01. August 2018. Available from: http://www.greenlightningresearch.com/pubs/GLR_paper_SRM-01.html

[13] Greatrix DR. Transient burning rate model for solid rocket motor internal ballistic simulations. International Journal of Aerospace Engineering. 2008;**2008**:826070

[14] Willcox MA, Quinn Brewster M, Tang KC, Scott Stewart D, Kuznetsov I. Solid rocket motor internal ballistics simulation using three-dimensional grain burnback. Journal of Propulsion and Power. 2007;**23**(3)